Hydraulic Fracturing-driven Infrasound Signals – A New Class of Signal for Subsurface Engineering

Aditya Chakravarty[1], Jordan Stenftenagel[1], Kan Wu[1], Benchun Duan[2], Siddharth Misra[1,2]

[1] Dept of Petroleum Engineering, Texas A&M University
[2] Dept of Geology and Geophysics, Texas A&M University

Corresponding author: Aditya Chakravarty (aditya.chakravarty@tamu.edu)

Key Points:

- Located the infrasound sources generated during hydraulic fracturing through cross correlation-based grid search.
- Analyzed the spatiotemporal evolution of the infrasound sources during the hydraulic stimulations and examined their relationship with concurrent microseismicity.
- Developed a conceptual model for infrasound generation that asserts the reopening of natural fractures as the key mechanism.

Abstract

Fluid injection into subsurface causes rock deformations, which give rise to mechanical waves in the surrounding rock. This article focuses on the infrasound signals (2-80 Hz) recorded by hydrophones during a meso-scale (~10 meter) hydraulic fracturing experiment at depth of 1.5 kilometer. We present a full-waveform-based data-driven workflow to map the spatiotemporal evolution of the infrasound sources produced during hydraulic fracturing. The infrasound source locations are compared against the simultaneously created microseismic source locations. Orientation of the infrasound source point cloud strongly agrees with natural fracture orientation, as inferred from the discrete fracture-network modelling. Finally, we arrive at a conceptual model of fluid-injection driven infrasound generation in subsurface and posit that the reopening of natural fractures is the main mechanism of the infrasound generation. A joint analysis of signals from microseismicity and infrasound sources can improve subsurface fracture imaging.

Plain Language Summary

Underground rocks break and vibrate like a giant subwoofer when fluids are pumped into the earth at sufficiently high injection rates. We analyzed the low-frequency component of recorded hydrophone signals to locate the infrasound energy sources and track their spatiotemporal evolution in the subsurface. These source locations highlight the sections of rock deformation not seen through traditional methods, like microseismic imaging. For imaging underground fracture networks, this new class of infrasound signals is complementary to using signals produced due to microseismicity. A new conceptual model of the fluid-injection driven infrasound generation is presented. The newly developed workflow can aid in imaging subsurface fluid pathways for geothermal and hydrocarbon resource development.

1 Introduction

A) Testbed and Experiment Description

The EGS Collab Experiment 1 is a meso-scale (~10 m) hydraulic fracturing testbed situated at the Homestake Gold Mine in Leads, South Dakota at a depth of 1.5 km. The aim of the experiment 1 is detailed characterization of hydraulic fracturing through dense geophysical instrumentation of the stimulated rock volume (Kneafsey et al., 2020 and Chakravarty and Misra, 2022). The passive microseismicity during hydraulic stimulation is recorded through array of accelerometers and hydrophones (Figure 1a). The located events determined through manual picking were refined by applying the PhaseNet picker (Zhu and Beroza, 2018) followed with the application of double difference relocation to obtain the final microseismic catalog (Schoenball et al., 2019 and Chai et al., 2020). This catalog, along with distributed fiber optic data and core measurements, which was used to further interpret the fracture network (Fu et al., 2021), constitutes the microseismic point cloud (Figure S7). In this work, we focus on the hydrophone measurements in the low frequency range (2-80 Hz); hereafter, refer as infrasound. Five injection experiments were conducted between 22 and 25 May 2018. The injection rate varied between 200 mL/min to 4.5 L/min. The injection and production wells were drilled in the direction of minimum horizontal stress. Table T1 (supplementary text) describes the experiments analyzed here. The hydrophones, spaced 120 centimeters apart, are grouted in place with cement on the monitoring wells. The hydrophones recorded emergent signals in the infrasound frequency (Figure 1c).

B) Monitoring the Fluid-Driven Low-Frequency Subsurface Deformations

Subsurface infrasound can be generated in a wide variety of geological settings where a fluid-driven volumetric process is involved, for example hydrothermal fluid circulation in volcanos, (e.g., Lehr et al., 2019), geysers (e.g., Nayak et al., 2020) and oceanic magmatism (e.g., Sgroi et al., 2009). Neimz et al., 2021 reported borehole tilt signals recorded by broadband seismometers during hydraulic fracturing at the Aspo Hard Rock Laboratory. The tilt magnitude was shown to be directly correlated with injected fluid volume. They concluded that joint analysis of tilt and microseismicity aided fracture growth monitoring. Low-frequency signals from rock deformations have been observed in similar meso-scale rock fracturing experiments like the Aspo Hard Rock Laboratory in Sweden (Zang et al., 2017) and the Grose-Schoen beck in Germany (Boese et al., 2022), and in field-scale hydraulic stimulations in tight sands (Das and Zoback, 2012). However, no further quantitative treatment has been extended for this class of signals so far. Our work focuses on the hydraulic stimulation experiments conducted on a notch located at depth of 50 m on the injection well (Figure 1b) in May 2018. The concurrent geophysical and geomechanical changes in the stimulated volume are captured through densely instruments monitoring boreholes equipped with distributed strain and temperature sensing,

electric resistivity, and borehole displacement sensors, apart from the hydrophone and accelerometer arrays.

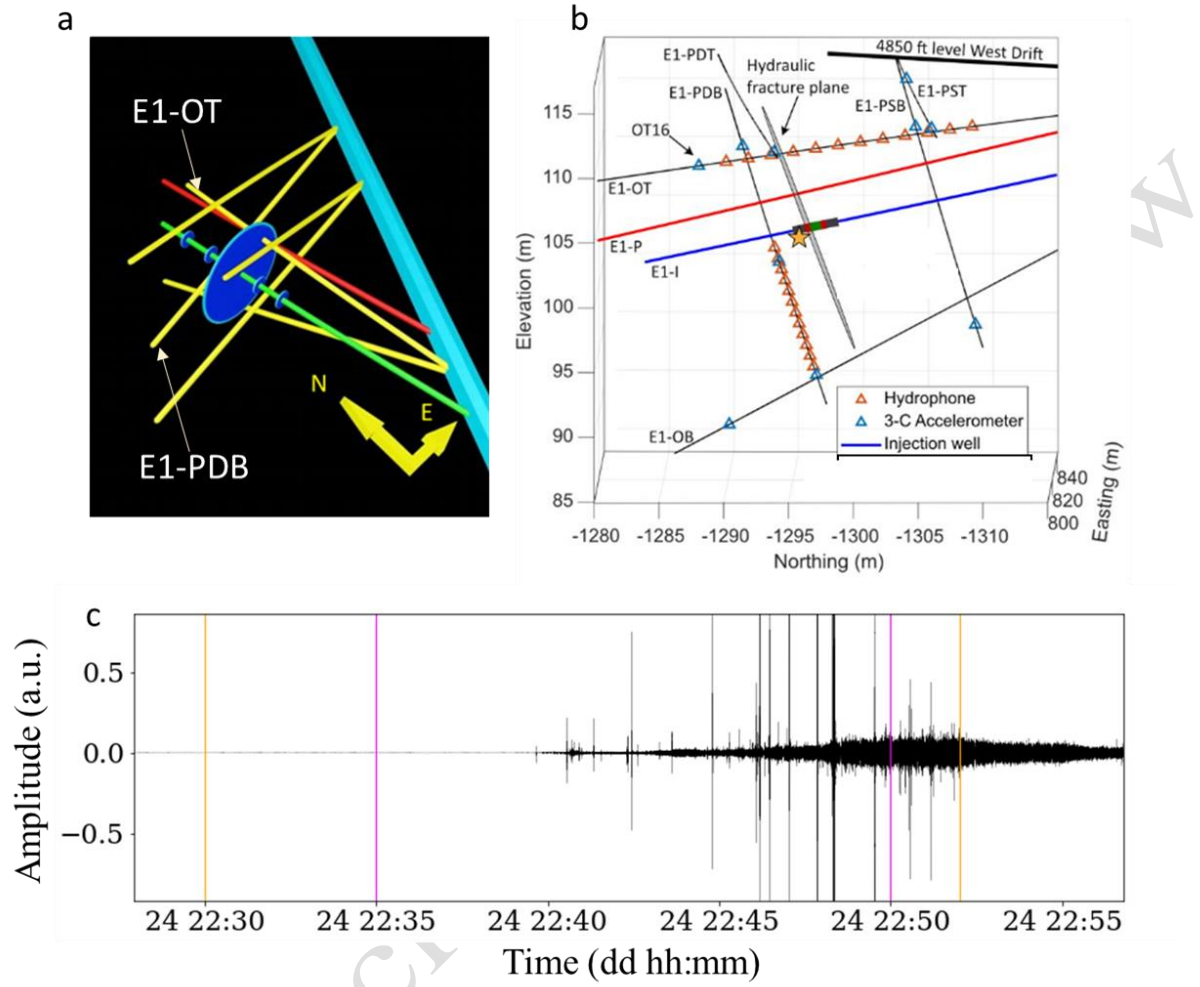

Figure 1 – a) Testbed layout of EGS Collab Experiment 1 in Homestake Mine in Leads, South Dakota. Inset shows the schematic of the well layout, situated at depth of 1500 meters. Red and green lines represent injection and production wells, respectively, drilled along the minimum horizontal stress direction. Thick cyan line represents the mine shaft. b) Hydrophone layout. c) infrasound (2-80 Hz) signal measured by hydrophone OT02 on the 24 May hydraulic fracture experiment. Time axis represents day: hour: minute. The emergent nature of individual signal pulses is visibly evident only at much finer time scales. Yellow and magenta vertical line on left show the start of injection and appearance of first microseismicity, and the other set of lines mark the last microseismic event and the end of fluid injection. The visible, larger-scale tremor signal monotonically increases till the pumping stops.

2 Methodology

A) Data Acquisition

The first step of analysis is the preprocessing of the hydrophone records. Two monitoring wells E1-OT and E1-PDB are equipped with High Tech HTI-96-Min hydrophones. Each well has 12 hydrophones spaced two feet apart (Figure 1B). This system has demonstrated high sensitivity in the 2-80 Hz range and applied for quantifying seismic wavefields in oceanic environments (Davidsen et al., 2019 and Lillis et al., 2018). The first step is preprocessing of the hydrophone records. Active seismic sources were being fired during fracturing process and have a very high relative amplitude that overwhelms the underlying passive signal if not clipped. Using the precise timings of active seismic firings, the corresponding time windows were zeroed out in the raw data and replaced with gaussian noise with central tendency statistics matching the neighboring data. As the signals of interest are not impulsive, the source locations identified using first arrival picking methods, like ratio of short-term average to long term average (STA-LTA), are rendered inaccurate. Instead, we located the sources of the fluid injection-driven infrasound using cross correlation-based analysis of full waveforms recorded by the hydrophone array. As the method is data-driven, several filters are applied to minimize the uncertainty associated with the sources.

B) Hydrophone Signal Processing

Following the concatenation and removal of active seismic signals, the signal is detrended and band passed to 2-80 Hz. Since the signals are emergent in nature, we used cross correlation-based grid search approach, which has been widely applied for locating tremor sources in regional and local scales (Wech and Creager, 2008). The input for the algorithm is hydrophone signal, a grid, and a velocity. For the grid dimensions, we used the extent of the hydrophone network with an extension of 30% length in both directions and used an isotropic velocity of 5.5 km/second for the compressional wave. A brief description of the rolling window location algorithm is as follows. At every given window, pairwise signals from every station are cross correlated i.e., their similarity is measured as function of displacement of one signal with respect to another. The observed travel time lag as calculated from the correlogram is compared against the calculated theoretical time lag between the station pair using an input velocity model. Within the grid search, the grid node yielding the minimum misfit between modelled and observed difference between objective functions is determined as the source location for the windowed signal. Given a suitable isotropic velocity model, the key parameters determining the source locations of the algorithm are the window length and window overlap. Determining the signal duration of emergent signals is nontrivial due to uncertainty in detecting first arrivals. Application of STA-LTA methods usually lead to overestimating the pulse duration. To get an estimate of the pulse duration, we applied the STA-LTA filter to a sample of hydrophone data from well E1-OT, and then corrected for the overestimation. An average value of one second was obtained as the average pulse duration of the infrasound signals (Figure S1). With this

information, a window length is 1 second and window overlap is 0.5 second is chosen for subsequent analysis.

C) Postprocessing Methods on the Grid Search Output

As the location techniqu is data driven, filters are needed to remove the false positives from results. The filtering steps are described as follows:

1.) Correlated noise signals can be highly correlated, which manifests as extremely high normalized cross correlation (CC) coefficients; therefore, the first filter is in form of upper bound of 0.95 on the cross-correlation value. Very loosely correlated signals, have low normalized cross correlation; hence, a lower bound of 0.6 is set. Both the correlated noise and uncorrelated signal windows will yield false positives in the cross-correlation based location. In summary, the windows having normalized cross-correlation coefficients outside the defined bounds (0.6-0.95) are discarded.

2.) The second filter is based on the array beam power (Kvaerna and Doornbos, 1985). Using the window lengths and window overlap as used in the location algorithm, the relative power of the hydrophone array was computed throughout the experiments. As a result, both the grid search-based location and beamforming outputs have identical timestamps. The located timestamps (through the grid search) that have normalized beam power lower than the noise floor of the beamforming output is discarded. A threshold value of relative power (0.3) effectively differentiated located and non-located timestamps. In other words, the locations which have a relative power lower the noise floor were removed. The differences between the beam power of the retained and discarded timestamps are shown in Figure S2.

3.) The third filter is based on bootstrapping. For every timestep, twenty iterations are performed for the cross-correlation-based locations and in every iteration 5 % of the cross correlograms are randomly removed, and the resulting scatter is considered a measure of location uncertainty. The data points with the highest 10 percent of the scatter values are discarded (for example, in Figure S3). The discarded points represent locations showing maximum scatter in determined locations.

4.) The last filter is based on the misfits obtained in the grid search algorithm. The misfit is defined as the difference between the maximum normalized cross-correlation (CC) function and the cross-correlation function corresponding to the located grid node. A large misfit implies weak support from the modelled time lag (from cross correlation) with the observed time lag. 50% of the data showing highest misfit values was discarded (Figure S4). Note that the spatial coverage of the source locations shows little change despite losing half the data, underscoring the effectiveness of the misfit filter (Figure S5).

3 Results and Discussion

Two orthogonal hydrophone strings, each consisting of 12 hydrophones recorded the infrasound and infrasound emission during fluid injections. The string E1-OT is perpendicular to the point cloud and intersected by it (Figure S7) whereas the string E1-PDB is sub parallel to the cloud and not intersected by it. As the hydrophones on the well E1-OT are at closer range to the fluid driven deformation, the incident infrasound signal intensity is greater on the E1-OT hydrophones. The signal energy recorded on the string E1-OT is roughly five orders of

magnitude greater than string E1-PDB. On 24 May the fluid injection caused hydraulic fracture propagation until the fracture intersected the production well. The microseismicity subsided as soon as the intersection with production well caused depressurization. In contrast, the stimulations of later experiments mostly involved fluid flow through a fractured volume, with a relatively lower rate of microseismicity. The change from fracture propagation to fluid flow through fracture is manifest in nature of the cumulative signal energy. Impulsive energy release indicative of stick slip type of fracture propagation is dominant on 24 May, wherein the energy release is in discrete bursts, resulting in strong ridges in the cumulative energy curves from all sensors (Figure 2, left). Fluid flow through fracture conduits generates long-period infrasound tremors, indicative of long duration energy release that result in progressively smoother cumulative energy release (Figure 2 C, D). A strong dependence of the cumulative injected volume with the cumulative signal energy was consistently observed (Supplementary Figure S6) that implies that the infrasound signals are generated from fluid driven processes. Note that both hydrophone strings, regardless of their distance from the microseismic cloud (our only proxy for the fracture location) show this behavior. This implies that although the string closer to the deformation records a much high energy, the nature of the energy recorded at different locations is consistent. In other words, both the blue and red curves (corresponding to strings OT and PDB respectively) have similar morphology while having different scale.

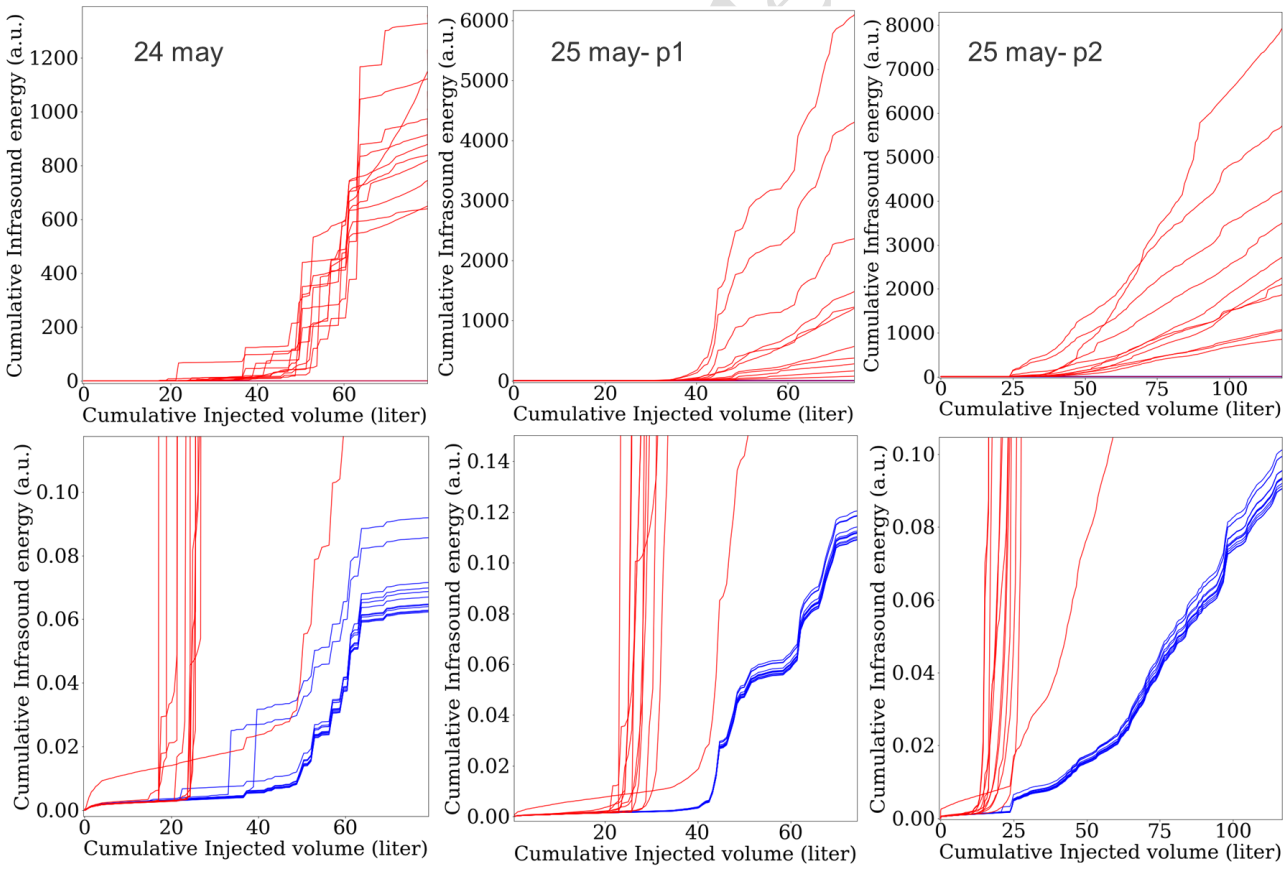

Figure 2: Dependence of fluid injection rate on infrasound energy release. E1-OT is situated perpendicular to the fractured zone and is intersected by it whereas E1-PDB is lies subparallel to the fracture and further away than E1-OT. The infrasound energy measured by E1-OT (red)

hydrophones is five orders of magnitude greater than the distant string E1-PDB (blue). Note that as the experiment proceeds, the gradient of cumulative infrasound energy for the both the hydrophone strings becomes progressively smoother. Impulsive energy release indicative of stick slip type of fracture propagation is dominant on 24 May, wherein the energy release is in discrete bursts, resulting in strong ridges in the cumulative energy curves from all sensors. Fluid flow through fracture conduits generates long-period infrasound tremors, indicative of long duration energy release. This transition suggests a regime change from fluid-driven fracture propagation to fluid flow through fractured conduits.

On 22 and 23 May the maximum injection rates were 200 mL/min and 400 mL/min respectively and only very weak infrasound signals were obtained. Signals with sufficiently high signal to noise ratio were obtained for 24 May, and the two parts of 25 May wherein the maximum injection rate was 4.5 L/min, the highest values in current experiment. Figure 3 shows the location of the infrasound sources. After applying the filters to the initial result from cross correlation-based grid search, a total of 322, 818, and 1117 infrasound source locations were obtained for the three stimulations respectively.

A) Spatiotemporal Evolution of Infrasound Sources and Microseismicity

Figure 3 shows the spatiotemporal evolution of the infrasound source locations. On 24th, early time (up to 22:40 UTC) sources spread perpendicular to the injection well (Figure 3a). Around 22:45 UTC, the sources are concentrated along a lineament sub parallel to the injection well. The later events are oriented along the same direction but have migrated northward from the injection point. Simultaneous microseismicity is shown in Figure 3b. The microseismic point cloud situated at x=815 m overlays and extends the late-time infrasound source point cloud which is situated north of the injection point. The sources on 25th part 1 (Figure 3c) show a less diffuse distribution than previously seen. The early time sources lie along an east-west trend (i.e., sub-perpendicular to injection well) south of injection point. A relatively sparse linear trend is also formed by later events on the north of injection point. Two subparallel lineaments in east-west direction are observed. At the start of injection on 25th part 2 (Figure 3e), infrasound sources fall

on the previously described two lineaments on either side of injection point, being sub perpendicular to the injection well. The latter events are aligned sub parallel to the injection well.

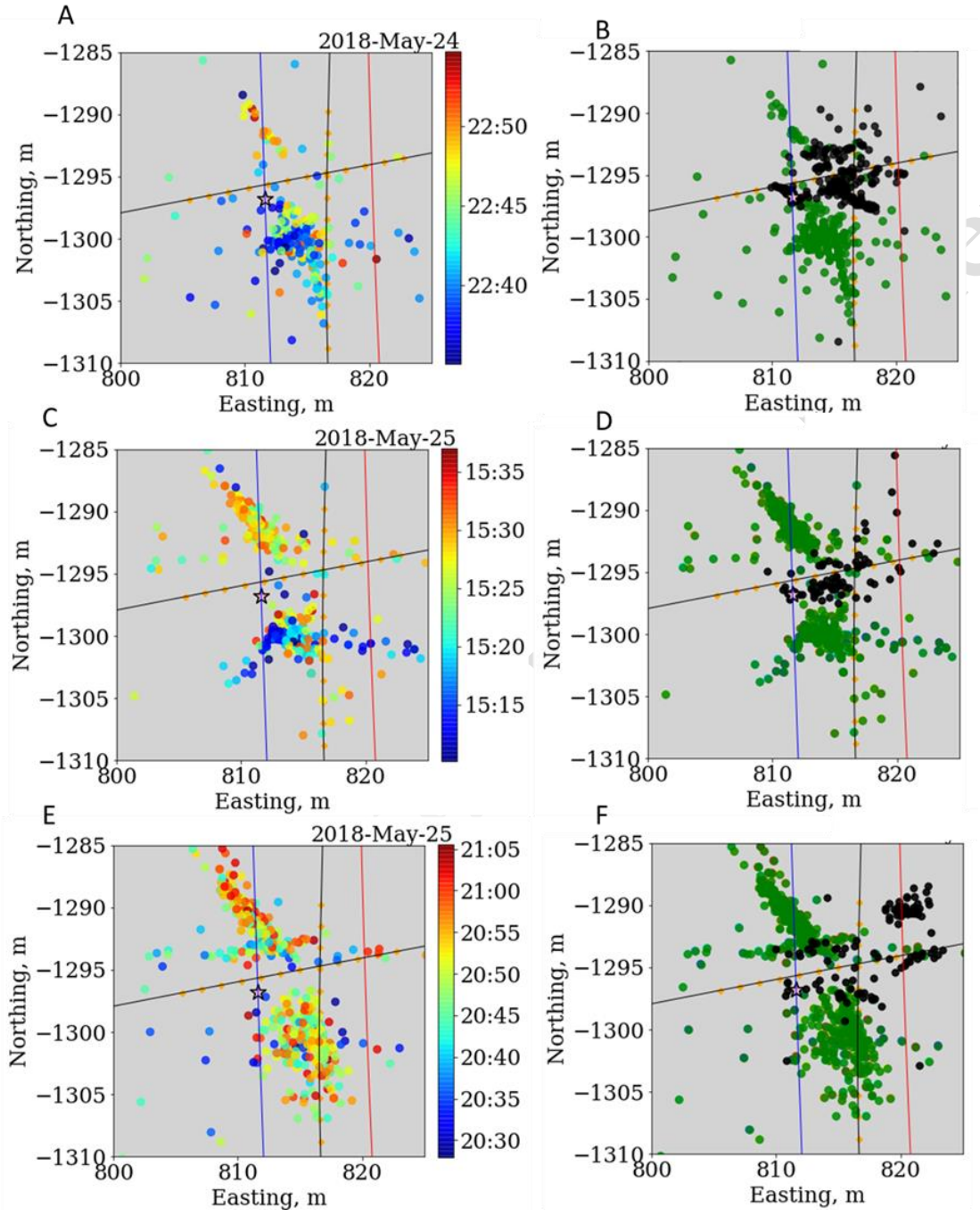

Figure 3: a,b) May 24; c,d) May 25 part 1; and e,f) May 25 part 2. Colored points show infrasound while black points show the simultaneously recorded microseismicity. Blue and red lines indicate injection and production wells respectively. Pink star on the injection well E1-I marks the injection point. Black line subparallel to injection and monitoring wells is hydrophone string E1-PDB, and sub horizontal line is string E1-OT. Orange squares overlain on lines mark the hydrophone sensors emplaced in the monitoring wells.

B) Joint analysis of Discrete Fracture Network and Infrasound Source Locations

Fusion of complimentary imaging methods like active and passive seismic can improve fracture imaging (e.g., Chakravarty and Misra, 2021). Similarly, the joint analysis of high and low frequency components of deformation captures information about fracture phenomena that is absent in those from standalone methods, such as microseismic analysis. The high frequency microseismicity usually corresponds to the shear slippage along the fractures leading to fracture propagation. In case of fluid injection-induced seismicity there is also a significant volumetric component in the seismic moment at much higher, microseismic frequency range, that is reflected by a significant percentage of the isotropic component in the microearthquake moment tensors (Martinez-Garzon at al., 2017). The lithology of the EGS Collab experiment 1 testbed is naturally fractured, highly metamorphosed phyllite. Whether intact or fractured, as fluid is pumped in a fractured rock, the injection causes crack opening. This pressurized fluid 'inflates' (or deflates, in case of drainage) the crack volume, the volume behaves like a diaphragm generating mechanical waves. Whereas in microseismicity, S-wave energy is predominantly generated, it is assumed that crack opening is dominantly tensile and generates P-wave energy. These low frequency P-waves are then recorded by the surrounding the array of pressure transducers. Using the example of fluid injection in a fractured rock, we present our conceptual model of fluid-driven infrasound generation in Figure 4a. In this model the fluid front is driving the fracture propagation as it shears the rock fabric, creating high-frequency shear motion (microseismicity). In the wake of the fluid front, the pressurized volume emanates low frequency P-waves.

The discrete fracture network showing the orientation and extent of the interpreted natural fractures is shown in Figure 4b. Dominant orientation of the fractures is 140° (CCW from east). These natural fractures, oriented subparallel to least horizontal stress direction (and the injection well) are the most favorable candidates for the fluid pressurization as described above (Figure 4c). The infrasound source cloud has two principal directions: dominant orientation being 140° (CCW from east) and the minor direction being the east-west trending section. The east west trending fracture network was created due to hydraulic fracturing, as shown in Figure 3b. We also note that a large section of the infrasound activity lies away from the production well. The difference in locations of microseismicity and infrasound underscore the different fluid pathways possible. The section described by microseismicity is where the critically stressed cracks are mobilized by fluid interactions, generating shear motion. On the other hand, sections of infrasound activity represent the pressurized zones, most likely reopened natural fractures, and generate low frequency compressional motion. Such observations also highlight the geometrical complexity of the stimulated rock volume in contrast to the ideal penny-shaped fracture as pictured in Figure 1a. Operationally, this observation corroborates high amounts of fluid leak off

into the fractured formation, seen from large differences between the injected and produced water volume.

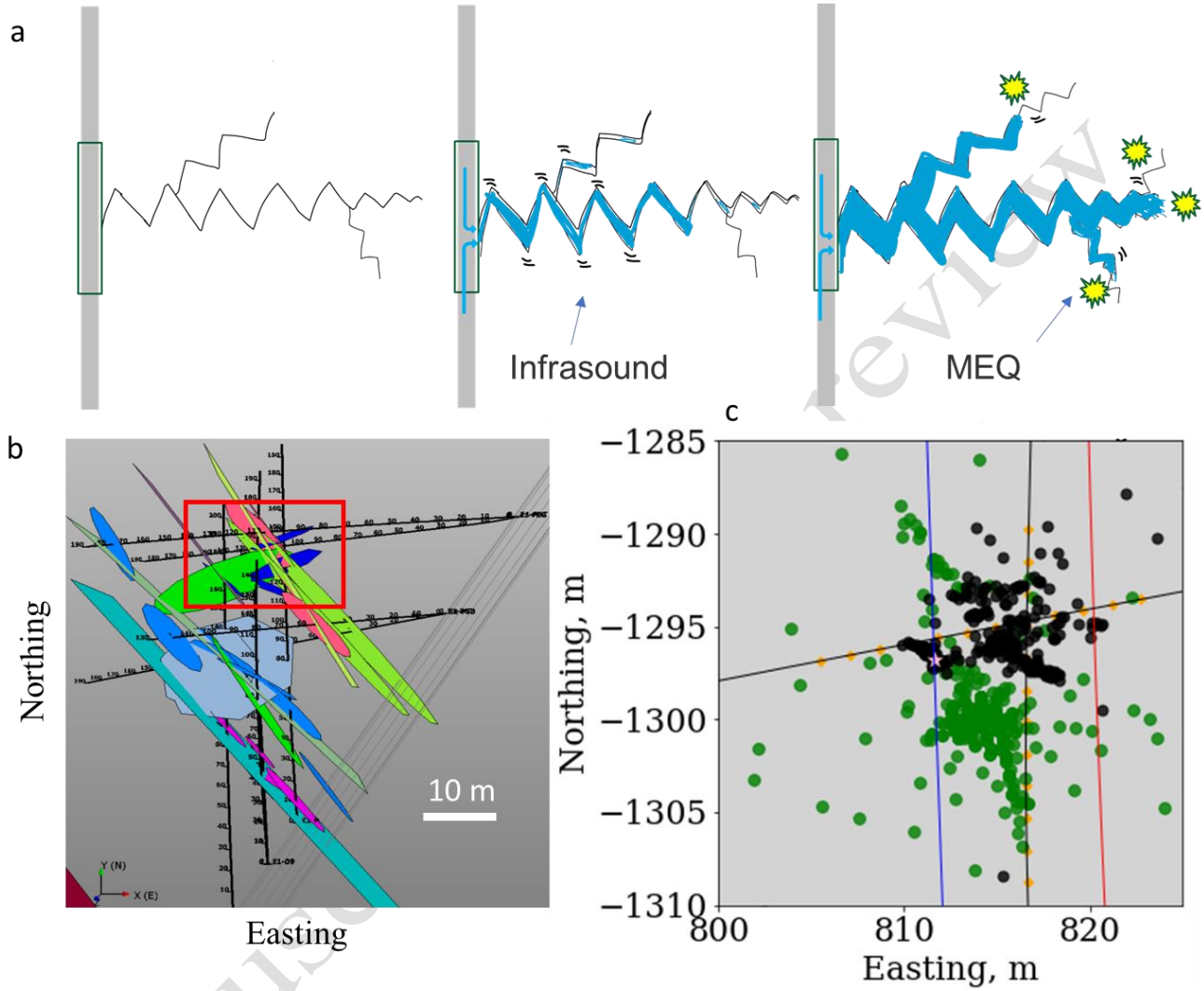

Figure 4: a) Schematic representation of the fluid-injection driven infrasound and microseismic energy release in a naturally fractured rock volume. MEQ's are microseismic events. b) Comparison with microseismic and discrete fracture network (DFN). The DFN figure is adapted from a model generated after the stimulation experiments (Schwering et al., 2019), wherein the authors used data from borehole optical and acoustic cameras to ascertain the dip, strike and aperture of the natural fractures encountered in the monitoring wells. The interpreted network shows the orientation of pre-existing natural fractures in the testbed, with large majority of the features inclined at 140° counterclockwise from east. Red box highlights the area of located infrasound activity. c) Their combined location cloud shows strong agreement with overall orientation inferred from the DFN.

4 Conclusions

The low-frequency (2-80 Hz) hydrophone signals captured during a 1.5 km deep meso-scale (~10 m) hydraulic fracturing experiment is analyzed to locate previously undetected infrasound sources. The infrasound detected by the hydrophone array is driven by fluid injection. A total of 322, 818, and 1117 infrasound source locations were obtained for the three stimulations respectively. Impulsive energy release at earlier stages corresponded to fracture propagation, while a smoother release at later stages of stimulation corresponds to tremor like motions generated from fluid flow in conduits. Infrasound signals of usable signal to noise ratio are produced only at relatively high fluid injection rates. The infrasound is emergent signal so first arrival picking from threshold-based methods is rendered inaccurate. Therefore, a data-driven cross-correlation-based grid search was applied to locate the infrasound source locations. Four filtering steps were designed and applied to improve the source location algorithm. The filters are thresholds based on the array power, thresholds based on the misfit in the cross-correlation based grid searching, scatter in locations obtained from station bootstrapping, and upper and lower bounds on the normalized cross correlation coefficient. Once the final locations of infrasound sources were obtained, the spatiotemporal evolution of the source locations over three episodes of fluid injection was analyzed. It is observed that the infrasound hotspots shifted around the fluid injection point over the course of fracturing operations. Whereas some locations produce exclusively one type of signal. Some locations can produce both infrasound and microseismicity. Those locations have overlap- show both high and low frequency deformation from fluid injection. Based on the spatiotemporal evolution of the infrasound sources in comparison to the microseismic sources and the discrete fracture network model, we conclude that the pressurized fluid inflates or deflates a fractured volume depending on whether there is injection or drainage- and the stimulated volume generates compressional waves.

Based on the discrete fracture network model of the testbed before fracturing, there exists a strong agreement between the fracture orientations and infrasound source locations. The pressurization of natural fractures appears to be the most likely mechanism for generating infrasound. As infrasound corresponds to fluid flow, our observations show that a large portion of the injected fluid is diverted away from the intended location i.e., the production well. A key caveat associated with our location method is that the output is in two dimensions.
It is well understood that microseismicity represents only a minuscule portion of the input hydraulic energy and only partly images the fracture network. The joint analysis of infrasound and microseismic encapsulates frequencies on the observable bounds of acquisition instrumentation (2 Hz to 15000 Hz). As a result, both high and low frequency fracturing phenomena driven by fluid injection are captured. The joint data reflects fluid injection-induced subsurface deformation that lies on a continuum - with one end representing of high frequency, small-scale shear slippage on fractures and the other end representing low frequency, large-scale void volume dilation or contraction. It is hence concluded that microseismicity and infrasound signals contain complementary information about rock deformation due to fluid injection, and their joint analysis renders a more complete picture of the stimulated fractures in subsurface.

Acknowledgments

This material is based upon work supported by the U.S. Department of Energy, Office of Science, Office of Basic Energy Sciences, Chemical Sciences Geosciences, and Biosciences Division, under Award Number DE-SC0020675 and the Texas A&M TRIAD funding. The authors acknowledge the efforts of the EGS collab team for conceptualizing and executing the experiments and hosting the open-source data. The authors are grateful to Texas A&M High Performance Research Computing staff for their support.

Open Research

The data used in this study is publicly available and can be accessed from the Geothermal Data Repository GDR (gdr.openei.org). The hydrophone, continuous microseismic data and microearthquake catalog are available at https://gdr.openei.org/submissions/1166. Hydraulic fracturing operational data is available at http://gdr.openei.org/submissions/1229. Data processing and visualization done in Python.

References

1. Boese, C. M., Kwiatek, G., Fischer, T., Plenkers, K., Starke, J., Blümle, F., Janssen, C., & Dresen, G. (2022). Seismic monitoring of the STIMTEC hydraulic stimulation experiment in anisotropic metamorphic gneiss. *Solid Earth*, *13*(2), 323–346. https://doi.org/10.5194/SE-13-323-2022

2. Chai, C., Maceira, M., Santos-Villalobos, H. J., Venkatakrishnan, S. V., Schoenball, M., Zhu, W., Beroza, G. C., & Thurber, C. (2020). Using a Deep Neural Network and Transfer Learning to Bridge Scales for Seismic Phase Picking. *Geophysical Research Letters*, *47*(16). https://doi.org/10.1029/2020GL088651

3. Chakravarty, A., & Misra, S. (2021). Hydraulic fracture mapping using wavelet-based fusion of wave transmission and emission measurements. Journal of Natural Gas Science and Engineering, 96, 104274. https://doi.org/10.1016/J.JNGSE.2021.104274

4. Chakravarty, A., & Misra, S. (2022). Unsupervised learning from three-component accelerometer data to monitor the spatiotemporal evolution of meso-scale hydraulic fractures. International Journal of Rock Mechanics and Mining Sciences, 151, 105046. https://doi.org/10.1016/J.IJRMMS.2022.105046

5. Das, I., & Zoback, M. D. (2013). Long-period long-duration seismic events during hydraulic stimulation of shale and tight-gas reservoirs - Part 2: Location and mechanisms. *Geophysics*, *78*(6).

6. Davidsen, J. G., Dong, H., Linné, M., Andersson, M. H., Piper, A., Prystay, T. S., Hvam, E. B., Thorstad, E. B., Whoriskey, F., Cooke, S. J., Sjursen, A. D., Rønning, L., Netland, T. C., & Hawkins, A. D. (2019). Effects of sound exposure from a seismic airgun on heart rate, acceleration and depth use in free-swimming Atlantic cod and saithe. *Conservation Physiology*, *7*(1). https://doi.org/10.1093/CONPHYS/COZ020

7. Fu, P., Schoenball, M., Ajo-Franklin, J. B., Chai, C., Maceira, M., Morris, J. P., Wu, H., Knox, H., Schwering, P. C., White, M. D., Burghardt, J. A., Strickland, C. E., Johnson, T. C., Vermeul, V. R., Sprinkle, P., Roberts, B., Ulrich, C., Guglielmi, Y., Cook, P. J., … Kneafsey, T. J. (2021). Close Observation of Hydraulic Fracturing at EGS Collab Experiment 1: Fracture Trajectory, Microseismic Interpretations, and the Role of Natural Fractures. *Journal of Geophysical Research: Solid Earth*, *126*(7), e2020JB020840. https://doi.org/10.1029/2020JB020840

8. Kneafsey, T. J., Blankenship, D., Dobson, P. F., Morris, J. P., White, M. D., Fu, P., et al. (2020). The EGS Collab Project: Learnings from Experiment 1. In Proceedings 45th 311 Workshop on Geothermal 312 Reservoir Engineering, 15 p., Stanford University, Stanford, California

9. Kvaerna T, D J Doornbos. An integrated approach to slowness analysis with arrays and three-component array data. Semiannual Technical Summary, 1 October 1985-31 March 1986. Kjeller, Norway: Sci. Rept. No. 2-85/86, NORSAR,1986.

10. Lehr, J., Eckel, F., Thorwart, M., & Rabbel, W. (2019). Low-Frequency Seismicity at Villarrica Volcano: Source Location and Seismic Velocities. *Journal of Geophysical Research: Solid Earth*, *124*(11), 11505–11530. https://doi.org/10.1029/2018JB017023

11. Lillis, A., Caruso, F., Mooney, T. A., Llopiz, J., Bohnenstiehl, D., & Eggleston, D. B. (2018). Drifting hydrophones as an ecologically meaningful approach to underwater soundscape measurement in coastal benthic habitats. *JEA*, *2*(1), 1–1. https://doi.org/10.22261/JEA.STBDH1

12. Martínez-Garzón, P., Kwiatek, G., Bohnhoff, M., & Dresen, G. (2017). Volumetric components in the earthquake source related to fluid injection and stress state. *Geophysical Research Letters*, *44*(2), 800–809. https://doi.org/10.1002/2016GL071963

13. Nayak, A., Manga, M., Hurwitz, S., Namiki, A., & Dawson, P. B. (2020). Origin and Properties of Hydrothermal Tremor at Lone Star Geyser, Yellowstone National Park,

USA. *Journal of Geophysical Research: Solid Earth*, *125*(12), e2020JB019711. https://doi.org/10.1029/2020JB019711

14. Niemz, P., Dahm, T., Milkereit, C., Cesca, S., Petersen, G., & Zang, A. (2021). Insights Into Hydraulic Fracture Growth Gained From a Joint Analysis of Seismometer-Derived Tilt Signals and Acoustic Emissions. *Journal of Geophysical Research: Solid Earth*, *126*(12), e2021JB023057. https://doi.org/10.1029/2021JB023057

15. Schoenball, M., Ajo-Franklin, J. B., Blankenship, D., Chai, C., Chakravarty, A., Dobson, P., Hopp, C., Kneafsey, T., Knox, H. A., Maceira, M., Robertson, M. C., Sprinkle, P., Strickland, C., Templeton, D., Schwering, P. C., Ulrich, C., & Wood, T. (2020). Creation of a Mixed-Mode Fracture Network at Mesoscale Through Hydraulic Fracturing and Shear Stimulation. *Journal of Geophysical Research: Solid Earth*, *125*(12), e2020JB019807. https://doi.org/10.1029/2020JB019807

16. Schwering, P. C., Doe, T. W., Roggenthen, W. M., Neupane, G. H., Johnston, H., Dobson, P. F., Ulrich, C., Singh, A., Uzunlar, N., and C. Reimers. "Deterministic Discrete Fracture Network (DFN) Model for the EGS Collab Project on the 4850 Level of the Sanford Underground Research Facility (SURF)." Paper presented at the 54th U.S. Rock Mechanics/Geomechanics Symposium, physical event cancelled, June 2020.
17. Sgroi, T., Montuori, C., Favali, P., & Agrusta, R. (2009). Low-frequency seismic signals recorded by OBS at Stromboli volcano (Southern Tyrrhenian Sea). *Geophysical Research Letters*, *36*(4). https://doi.org/10.1029/2008GL036477

18. Wech, A. G., & Creager, K. C. (2008). Automated detection and location of Cascadia tremor. *Geophysical Research Letters*, *35*(20), 20302. https://doi.org/10.1029/2008GL035458

19. Zang, A., Stephansson, O., Stenberg, L., Plenkers, K., Specht, S., Milkereit, C., Schill, E., Kwiatek, G., Dresen, G., Zimmermann, G., Dahm, T., & Weber, M. (2017). Hydraulic fracture monitoring in hard rock at 410 m depth with an advanced fluid-injection protocol and extensive sensor array. *Geophysical Journal International*, *208*(2), 790–813. https://doi.org/10.1093/GJI/GGW430

20. Zhu W, Beroza GC. PhaseNet: A deep-neural-network-based seismic arrival-time picking method. Geophys J Int. 2019;216(1):261-273. doi:10.1093/gji/ggy423